

Discriminating β , α and α'' phases in metastable β titanium alloys via segmentation: A combined electron backscattering diffraction and energy-dispersive X-ray spectroscopy approach

Frank Niessen^{1,*}, Azdiar A. Gazder¹

¹*Electron Microscopy Centre, University of Wollongong, New South Wales 2500, Australia*

Abstract

Annealed metastable β titanium (Ti) alloys comprise body-centred-cubic β and hexagonal-close-packed α phases and possibly, orthorhombic α'' martensite that forms on quenching or deformation. Electron backscattering diffraction is amongst the most popular methods for characterising such multi-phase microstructures. However, the crystallographic similarity between α and α'' martensite renders unambiguous discrimination of these phases via electron backscattering patterns (EBSPs) virtually impossible; thereby limiting the use of EBSD in characterising β -Ti alloys. In this study, we demonstrate that α and α'' martensite are primarily misindexed due to an indiscernible difference between these phases along their $[1\bar{1}0]_{\alpha}$ and $[010]_{\alpha''}$ zone axes. Furthermore, the slight compositional difference between α and α'' is insufficient to discriminate these phases using on-the-fly energy-dispersive X-ray spectroscopy (EDS) spectrum matching. Consequently, a segmentation method was developed that relies on a combination of reindexed EBSPs and grain-median EDS elemental data to unambiguously discriminate β , α and α'' martensite in metastable β Ti alloys. All steps are implemented in an open-source and freely available computer program called *phaseSegmenter* that makes use of the MTEX toolbox in MATLAB. The program is readily applicable to Ti alloys containing α' , α'' or massively transformed α as well as other phase transforming alloy systems with similar phase discrimination issues.

Keywords: electron backscattering diffraction (EBSD); energy-dispersive X-ray spectroscopy (EDS); phase segmentation; titanium; martensite

*Corresponding author, Contact: contact@fniessen.com

Post-print – Cite work as: [F. Niessen, A. A. Gazder, Discriminating β , α and α'' phases in metastable β titanium alloys via segmentation: A combined electron backscattering diffraction and energy-dispersive X-ray spectroscopy approach, Ultramicroscopy, 2020, DOI: 10.1016/j.ultramic.2020.112943]

1 Introduction

Titanium (Ti) alloys are in high commercial demand and are attracting increasing research interest. For the period 2018 – 2023, the compounded annual growth rate of the global titanium metal market is forecast at ~6 % p.a. [1]. Mimicking this commercial trend, the number of titanium-related research papers published in 2018 was 53 % higher compared to 2010[†] [2]. Traditionally, the attractive properties of Ti alloys have been outweighed by their high extraction and fabrication costs. The recent increase in popularity of Ti alloys is primarily driven by the cost reductions from the introduction of new fabrication methods [3,4].

Based on some early studies conducted in the 1960's [5,6], the fundamentals of transformation-induced plasticity were established in the late 1980's [7]. In turn, this laid the foundation for the design of transformation and/or twinning -induced plasticity (TRIP/TWIP) steels in the early 2000's [8]. These advanced high-strength steels make use of the TRIP/TWIP effects to extend material work-hardening to produce large gains in strength and ductility [9]. The commercial success of TRIP/TWIP steels gave clear incentives to extend this promising materials design concept to Ti alloys as well [10]. Although the development of TRIP/TWIP Ti alloys is still in its infancy, some promising Ti alloys showing both TRIP and TWIP effects have been designed and characterised to-date [11–13].

Since the morphology, size and orientation of the martensitic transformation product(s) forming within the parent phase of a TWIP/TRIP alloy directly affects the mechanical properties, it is crucial to unambiguously discriminate and characterise all phases. In TRIP steels, the parent phase is face-centred-cubic (*fcc*) austenite and the transformation product is body-centred-tetragonal (*bct*) martensite. The clearly distinct crystal structures of the parent and daughter phases and the scale of the microstructure made electron backscattering diffraction (EBSD) one of the preferred methods to confidently and quantitatively characterise such microstructures [14–19]. On the other hand, the similarity in the crystal structures of martensite and possible tertiary phases such as body-centred-cubic (*bcc*) ferrite and/or tempered martensite (*bcc* or *bct*) renders diffraction-based phase segmentation difficult. In such cases, other metrics like the characteristic grain size and shape [20]

[†] This figure concerns research papers indexed on ScienceDirect and is corrected for the overall increase in annually published research papers.

or the metrics of the electron backscatter pattern (EBSP) such as the band contrast, image quality [20], band slope [20,21] or confidence index [22] have been successfully utilised to segment the phases. The second author of this paper has provided a comprehensive summary of existing approaches to phase segmentation in advanced high strength steels (Ref. [23] and the references therein) and presented a correlative approach using EBSD and the carbon-K signal from energy dispersive X-ray spectroscopy (EDS) to unambiguously segment austenite, polygonal ferrite, martensite, bainitic ferrite and granular bainite.

In Ti alloys, the unambiguous indexing and subsequent characterisation of martensitic transformation products via EBSD is complicated by the crystallographic similarity of the daughter phases with the hexagonal closed-packed (*hcp*) α phase. Here, a metastable parent *bcc* β phase may form hexagonal closed-packed (*hcp*) α' or orthorhombic α'' during quenching or deformation. The occurrence of these martensitic phases depends on the overall stability of the parent β phase. While a less stable β phase results in the formation of α' , increasing β stability leads to the formation of orthorhombic α'' ; with the latter phase commonly perceived as an incomplete martensitic transformation to α' . In rare cases, both α' and α'' can form from the same parent β phase [24]. In additively manufactured or as-welded microstructures, cooling rates may be high enough to form the α phase by a massive transformation. In such reports, α' is similar in chemical composition to the *hcp* α phase; with the only difference between the two phases being the globular morphology of α [25–27]. In summary, the martensitic phases α' and α'' and massively formed α are crystallographically analogous to the α phase that develops during annealing below the β -transus temperature. The latter often co-exists with the β phase prior to a potential martensitic transformation.

Since α forms by a nucleation and growth process in the β matrix via the partitioning of solutes, it has a distinct chemical composition. On the other hand, α' , α'' and massively formed α form via a displacive mechanism from the parent β phase. However, due to the limitations imposed on the simultaneous EDS-EBSD technique by previous generation hardware, the small compositional differences comprising a few atomic percent in the four alloying elements (see Section 4.4) between α and the martensitic phases cannot be exploited to discriminate them on-the-fly during map acquisition or subsequently, using pixel-based, post-processing segmentation techniques. Consequently, in the following sections, we introduce a new phase segmentation method that reindexes EBSPs and utilises grain-median elemental data to unambiguously discriminate the β , α

and α'' phases in a 1023 grade metastable β Ti alloy. Finally, we discuss alternative strategies that may discriminate the phases and the applicability of the proposed segmentation method to Ti alloys.

2 Experimental methods

2.1 Material, heat treatment and specimen preparation

The nominal composition from glow-discharge optical emission spectroscopy of the 1023 grade metastable β Ti alloy of this study is Ti-9.5V-2Fe-3.1Al-0.015C-0.10-0.007N wt.%. Martensitic transformation from parent β to daughter α'' may result in up to 6 different martensitic orientation variants [28]. In the present alloy, thermally induced α'' martensite tends to form all 6 differently oriented variants in a single parent β grain whereas deformation-induced α'' martensite forms only those variants that favourably accommodate the applied macroscopic stress. Consequently, we chose a microstructure containing thermally induced α'' martensite in order to highlight orientation-dependent indexing issues and the robustness of the new phase segmentation method in discriminating α'' . The new phase segmentation method is however equally valid for both, thermally and deformation induced martensite.

A $12 \times 2 \times 2$ mm³ sample was wire-cut from a billet and sealed in an evacuated quartz tube capsule. The capsule was solution treated at 850 °C for 840 s to fully transform the sample microstructure to β , then cooled to 700 °C and annealed for 500 s to form 5-10 vol.% of α . Following this, the capsule was broken and the sample immediately water quenched. The quenching treatment led to the formation of α'' . The martensite start (M_s) temperature was estimated using the model in Ref. [10] in conjunction with the low-temperature thermodynamics database TiGen [10] and the computational thermodynamics software Open Calphad [29]. The computed M_s temperature was 61 °C. The lattice parameters of the three phases were determined by neutron diffraction and are provided in Table 1. The specimen was mechanically ground using 1200, 2400 and 4000 grit silicon carbide papers and electropolished at room temperature on a Struers Lectropol-5 using an electrolyte of 600 ml methanol + 360 ml butoxyethanol + 60 ml perchloric acid at 45 V, ~1.2 mA for 30 s.

Table 1: Lattice parameters of the unit cells of the analysed phases

Phase	Crystal structure	a [Å]	b [Å]	c [Å]	α [°]	β [°]	γ [°]
β	body-centred-cubic	3.241	3.241	3.241	90	90	90
α	hexagonal-close-packed	2.936	2.936	4.688	90	90	120
α''	orthorhombic	3.019	4.905	4.617	90	90	90

2.2 Orientation and compositional mapping

While the segmentation method to discriminate α and α'' is undertaken during post-processing, there are important experimental pre-requisites to fulfil in order to obtain a suitable dataset. For instance, since the segmentation method utilises EDS elemental maps, it is essential to simultaneously record the EDS signal during EBSD map acquisition. Moreover, to enable the reindexing of EBSPs, it is also essential to store all EBSP images.

Simultaneous EDS and EBSD mapping was undertaken on a JEOL JSM-7001F field emission gun - scanning electron microscope equipped with an Oxford Instruments Nordlys-II(S) EBSD detector and an 80 mm² X-Max EDS detector interfacing with the AZtec v4.1 acquisition software suite. All acquisition and processing parameters are summarised in Table 2.

3 Experimental results and analysis

3.1 Microstructure

At first glance, the forward-scatter electron image in Figure 1a shows the presence of two phases with α appearing raised and bright at the boundaries of and within individual grains of the darker β matrix. However, closer inspection reveals a weak, darker contrast within the β matrix; alluding to the presence of thermally induced α'' martensite with lenticular morphology. The location and morphology of the three phases is shown in greater detail in the band contrast map in Figure 1b. Band contrast defines the average intensity of the Hough peaks of an EBSP after greyscaling and binning to a bit range between 0 (black) to 255 (white). It follows that structures with elastically distorted lattices, higher crystalline defects or residual stresses (for example, caused by martensitic transformation) present with blurred Kikuchi band edges, diffuse Hough peaks and appear darker with lower band contrast values [23]. In accordance with this, Figure 1b shows that the parent β matrix and α have the highest band contrast values and appear brighter whereas the clearly

delineated α'' martensite tends to have lower band contrast values resulting in darker variations in greyscale. α'' martensite is fine-grained, has a lenticular morphology and shares common boundary interfaces with the parent β matrix but none with α .

Table 2: EBSD and EDS acquisition and processing parameters[‡]

Microscope settings	
Beam energy:	20 keV
Beam current:	~6.5 nA
Working distance:	15 mm
Specimen tilt:	70°
EBSD map acquisition parameters	
Mapped area:	180 × 150 μm^2
Step size:	100 nm
Acquisition rate:	40.5 Hz
EBSP resolution:	336 × 256 pxs ²
Camera exposure time:	9.26 ms
Camera gain:	High
Frame averaging:	1
EBSP processing parameters	
Hough resolution:	60
Number of detected bands:	11
Indexing mode:	Refined accuracy
EDS parameters	
EDS process time:	3
Energy range:	20 keV
EDS map type:	Processed (TruMap™) [30]
Detector deadtime:	50 – 55 %
Average spectrum count:	956

[‡] Some parameters are specific to the applied acquisition software AZtec 4.1 by Oxford Instruments.

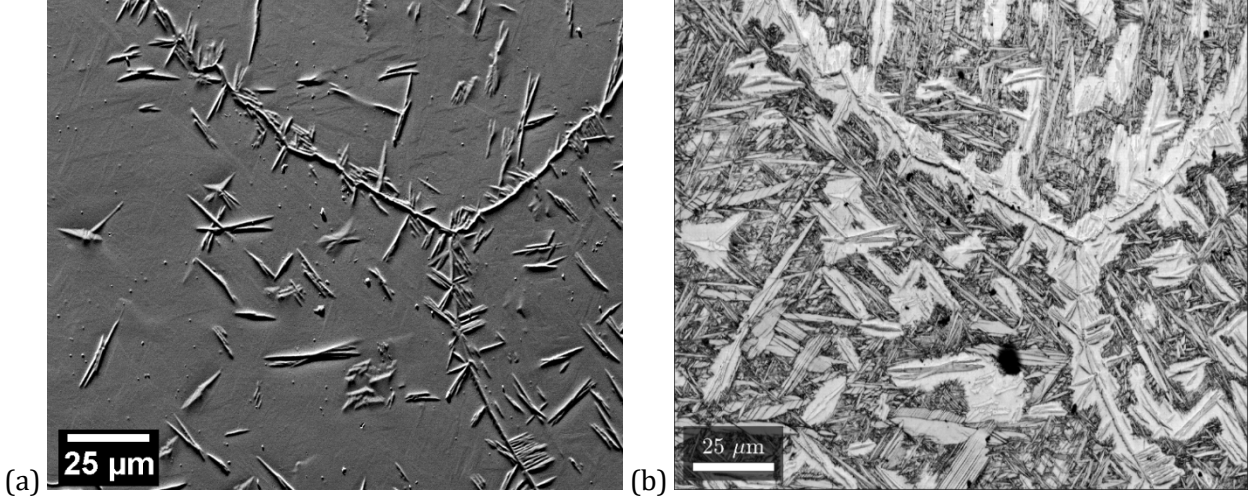


Figure 1: (a) Forward-scatter electron image showing bright α grains in a darker β matrix. α mainly precipitated at the β grain boundaries, which form a triple junction. A weak contrast within β indicates the formation of α'' martensite. (b) Band contrast map showing high band contrast in the β matrix and within α and low band contrast within thermally induced α'' martensite regions.

3.2 Orientation indexing

The maps in Figure 2 show orientation and phase data in the as-acquired (unprocessed) state with the EBSPs indexed using the parameters given in Table 2. Figure 2a is the all Euler map showing the orientation of individual crystal unit cells with respect to the specimen coordinate system by colour-coding the three Euler angles ϕ_1 , Φ and ϕ_2 as red, green and blue, respectively, in accordance with Bunge's notation [31]. This map type is suitable to show the orientations of multi-phase microstructures without using phase specific colour keys. Figure 2b is a higher magnification map of the area marked by the rectangle in Figure 2a. The grains appear to be consistently indexed with only a few unindexed points (or zero solutions) within them. Expectedly, most unindexed points are in the vicinity of boundary interfaces surrounding the small, lenticular grains of α'' martensite.

3.3 Phase indexing

Comparing Figure 1 with the phase map (Figure 2c) shows that while β and α are generally correctly indexed, a substantial fraction of α'' martensite is misindexed as α . Closer inspection of the quality of phase discrimination in the magnified area of Figure 2c shows that α'' grain interiors are not consistently discriminated as α'' by the indexing algorithm (Figure 2d). In most cases, α'' is

misindexed as α . However, in fewer cases, α is misindexed as α'' ; albeit far less frequently. Furthermore, while all α'' grains are misindexed as α to varying extents, Figure 2b and Figure 2d show that α'' grains with Φ close to 90° and small values of ϕ_1 and ϕ_2 (green colour) are more likely to be misindexed as α compared to other α'' grains.

3.4 Crystallography of α'' and the origin of phase misindexing

Since the comparison of Figure 2b with Figure 2d indicates an orientation dependence on the misindexing of α'' as α , EBSPs of particularly poorly indexed orientations were examined to identify the source of this error. Poorly indexed orientations were generally associated with EBSPs containing the $[010]_{\alpha''}$ zone axis (being equivalent to the Euler angles of $\phi_1 \sim 0^\circ$, $\Phi \sim 90^\circ$, $\phi_2 \sim 0^\circ$). An example of just such an EBSP obtained from the position marked by a black cross in Figure 2d is shown in Figure 3a. The quality of the greyscale contrast of the EBSP is ideal for indexing and is representative of α'' martensite in the dataset. Figure 3b and 3c show that this EBSP can be indexed by the OI's conventional Hough transformation algorithm as either α or α'' , respectively, without any discernible misfit. Therefore, it is unlikely that poor quality EBSPs are the reason behind the misindexing of α'' martensite.

In order to rationalise the source of this error, the crystallographic differences in the unit cells of orthorhombic α'' and hcp α need careful consideration. Orthorhombic α'' martensite is the result of an incomplete transformation to hcp α' martensite which in turn, has the same crystal structure as α . In this regard, it should also be noted that this orthorhombic crystal structure deviates only slightly from hexagonal symmetry [32,33]. Based on cubic and hexagonal axes conventions (see Table 1), the $[100]_{\alpha''}$, $[010]_{\alpha''}$ and $[001]_{\alpha''}$ zone axes directly correspond to the $[110]_\alpha$, $[\bar{1}10]_\alpha$ and $[001]_\alpha$ zone axes, respectively. Consequently, Figure 3b and c show that the $[010]_{\alpha''}$ and $[110]_{\alpha''}$ zone axes in α'' martensite are erroneously indexed as the $[\bar{1}10]_\alpha$ and $[010]_\alpha$ zone axes of α .

φ_1 : Φ : φ_2 :

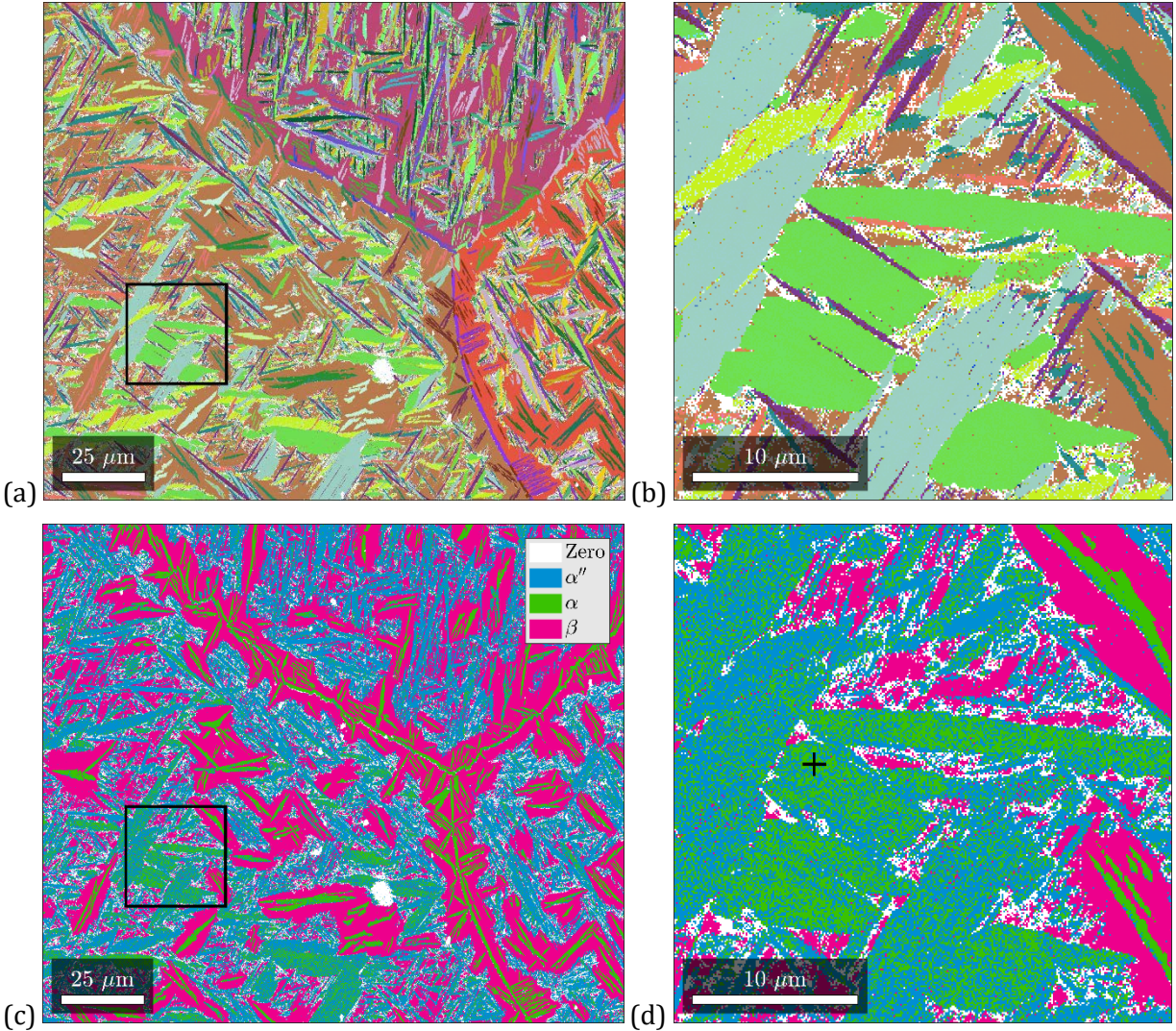


Figure 2: Unprocessed orientation data of the (a) Euler map showing the crystal orientations independent of phase indexing. The colour key shows the proportion of Euler angles φ_1 , Φ and φ_2 defined using red, green and blue channels, respectively. (b) Magnified area of the rectangle in Figure 2a showing coherent crystal orientations within particular grains. (c) Phase map of β , α and α'' and unindexed points (or zero solutions). It is evident that α'' is commonly misindexed as α . (d) Magnified area corresponding to area in Figure 2b showing detailed view of misindexing of α and α'' . It appears that certain α'' orientations are more prone to be misindexed as α . Even less prone α'' orientations and α grains show some level of misindexing. The cross marks the position of the EBSPs in Figure 3.

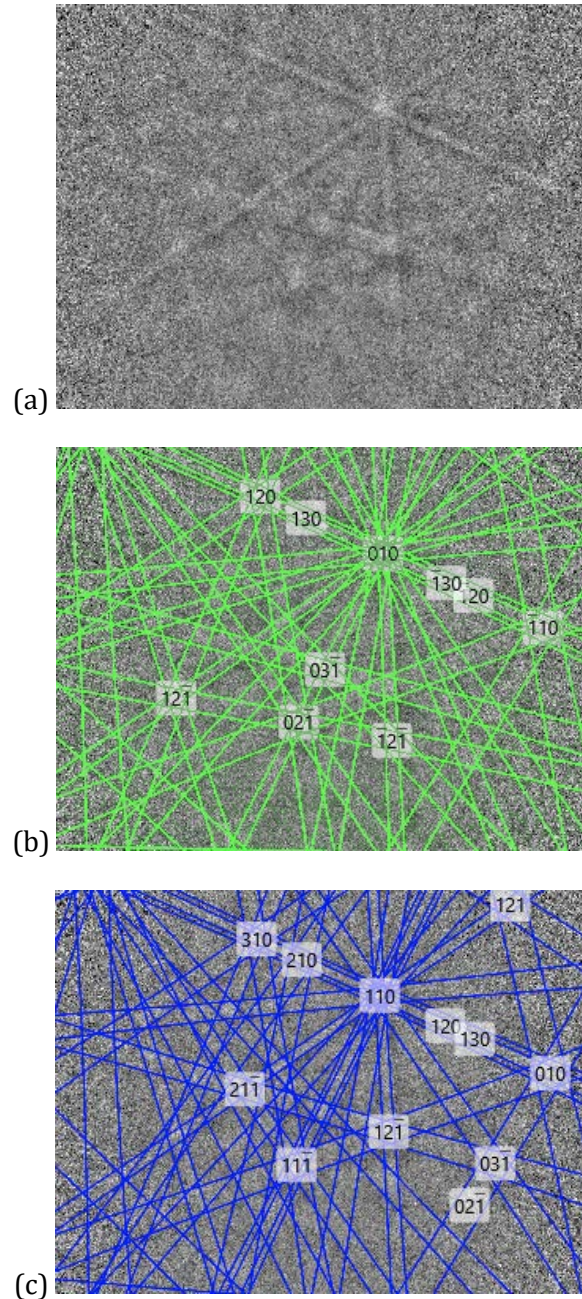


Figure 3: EBSPs from the marked position in Figure 2d. (a) Unindexed EBSP, EBSP indexed as (b) α and (c) α'' . In (b) and (c), it is evident that the $[010]_{\alpha''}$ and $[110]_{\alpha''}$ zone axes are misindexed as $[\bar{1}10]_{\alpha}$ and $[010]_{\alpha}$, respectively. Although the EBSP belongs to α'' , the indexing algorithm suggests both α or α'' as viable solutions because no misfit is discerned for either phase.

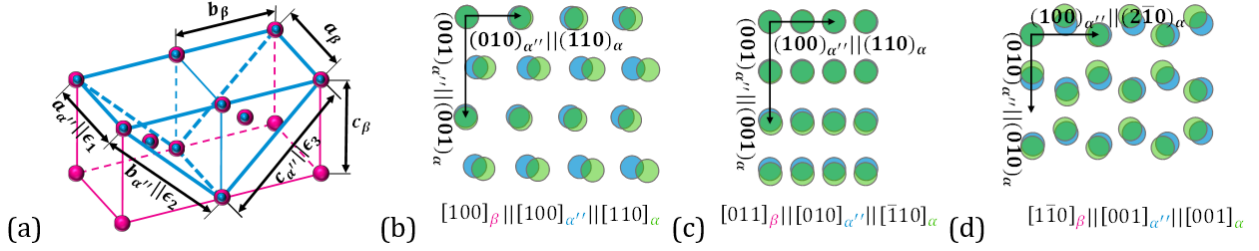


Figure 4: (a) Schematic showing the lattice correspondence of two β unit cells and half of the α'' unit cell indicating the axes of the principal lattice strains ϵ_1 to ϵ_3 . (b - d) Superimposed 2-dimensional projections of the α (green) and α'' (blue) crystal lattices from Table 1 along the three unit cell axes of α'' : Zone axes (b) $[110]_\alpha$ and $[100]_{\alpha''}$, (c) $[1\bar{1}0]_\alpha$ and $[010]_{\alpha''}$ and (d) $[001]_\alpha$ and $[001]_{\alpha''}$. Only the projections along the $[100]_{\alpha''}$ and $[001]_{\alpha''}$ zones axes reveal the atomic shuffle that discerns α'' from α and α' .

The first component of the atomic displacements involved in the incomplete orthorhombic α'' or hexagonal α' martensitic transformation from β is a homogeneous lattice strain. This lattice strain is equal for both, α' and α'' martensite, and is commonly referred to as the Bain strain [32]. It consists of a negative principal strain along $[100]_{\alpha''}$, a positive principal strain of similar magnitude along $[010]_{\alpha''}$ and an approximately tenfold in magnitude smaller principal strain along $[001]_{\alpha''}$ [32,34,35]. The principal strains are schematically shown with reference to the β and α'' lattice correspondence in Figure 4a. The second component of the atom displacements involved in the hexagonal α' martensitic transformation is a $\{1\bar{1}0\}\langle 110 \rangle_\beta$ atomic shuffle [36]. In the case of the orthorhombic α'' martensitic transformation, this atomic shuffle is incomplete; such that it provides the only major distinction between α'' martensite and the hexagonal α and α' crystal structures.

Figure 4b to 4d show superimposed projections of the α and α'' crystal lattices along the $\langle 100 \rangle_{\alpha''}$ zone axes, which are based on the crystallographic parameters in Table 1 and created by analysing the closely-related unit cells with the crystallographic toolbox CrysTBox [37]. The incomplete atomic shuffle of the β to α'' martensitic transformation is most apparent in the $[100]_{\alpha''}$ projection, where atoms are displaced from an initially columnar arrangement towards the hexagonal positions along $[010]_{\alpha''}/[0\bar{1}1]_\beta$ on every other $(001)_{\alpha''}/(011)_\beta$ plane. The atomic shuffle is also noticeable in the $[001]_{\alpha''}$ projection (Figure 4d). However, and most importantly, the shuffle is indiscernible in the $[010]_{\alpha''}$ projection (Figure 4c), which only shows a slight homogeneous difference in planar spacing of < 3%. In this projection, the $[010]_{\alpha''}/[0\bar{1}1]_\beta$ atomic shuffle occurs in the out-of-plane direction

and is thus indiscernible. Consequently, the source of the error leading to the misindexing of α'' martensite as α is mainly found in EBSPs containing the $[010]_{\alpha''}$ zone axis. Along this projection, the atomic shuffle of α'' martensite, which is the only discernible marker distinguishing α from α' , is invisible.

4 Phase segmentation method

Section 3.2.3 shows that the detection of the atomic shuffle is critical to unambiguously discriminate α'' martensite from α (or α'). However, since commercial EBSD indexing algorithms mainly rely on interplanar angles rather than planar spacings [38] and the crystallographic difference between α'' martensite and α is indiscernible along their $[\bar{1}10]_\alpha$ and $[010]_{\alpha''}$ zone axes, EBSPs alone cannot provide the means to unambiguously discriminate these phases. Moreover, as the detected differences in elemental composition between α and $\beta + \alpha''$ is small and only comprises a few atomic percent for the four alloying elements (see Section 4.4), these phases cannot be consistently discriminated by: (i) on-the-fly during map acquisition or, (ii) subsequently, using pixel-based, post-processing segmentation techniques. We therefore need to consider a phase segmentation procedure that reindexes EBSPs and confidently delineates regions of elemental difference between the phases using a grain-median approach. This combined post-processing approach provides the most unambiguous means to discriminate all three phases.

In the following paragraphs, the phase segmentation method is briefly summarised at first, followed by a more detailed description of the individual steps. The latter also includes remarks on the functionality of the open-source and freely available program *phaseSegmenter* [39] written in MATLAB [40]. The program utilises the functions and data-processing capabilities of the MTEX toolbox [41].

4.1 Overview

As detailed in Section 3, the investigated microstructure comprises three phases, namely β , α and α'' . Of these three phases, only β can be unambiguously identified using EBSP. Since α forms by a nucleation and growth process in the β matrix via the partitioning of solutes, the former phase has a compositional difference from the latter. On the other hand, since α'' forms from β by a displacive martensitic transformation during quenching (or deformation), this phase has the same chemical composition as its parent β . It is therefore the distinct crystal structure of β and the distinct

composition of α that will be taken advantage of during segmentation in order to unambiguously discriminate all three phases.

A detailed flowchart describing the steps involved in this phase segmentation method is shown in Figure 5. The method is subdivided into steps that are conducted in: (1) OI Aztec, (2) OI Channel-5, and (3) the MATLAB-based *phaseSegmenter* program. The sub-steps during acquisition (1) and post-processing (2 and 3) are indicated by letters.

After the simultaneous EDS-EBSD maps are acquired and the EBSPs saved (Figure 5, 1.a), the procedure begins with reindexing the EBSPs twice over in OI Aztec using both, β and α for the first map and only α'' martensite for the second map (Figure 5, 1.b).

In the first map, the α -indexed pixels denote both, genuine α grains and misindexed α'' grains. This first map is imported into *phaseSegmenter* (Figure 5, 3.a), the grains of the α -indexed pixels are computed, and the median EDS count of a characteristic alloying element is assigned to each grain (Figure 5, 3.b). The latter is used to segment α from α'' martensite.

A threshold value of the grain-median EDS counts of a characteristic alloying element is then used to threshold the pixels contained within all α -indexed grains in order to segment α (Figure 5, 3.c). Since β is correctly discriminated beforehand and α is now segmented, the remaining pixels belong to α'' martensite (and/or unindexed points). Consequently, in the last step, the phase and orientation data of the pixels belonging to α'' martensite in the first map are replaced by those contained in the second map (Figure 5, 3.d). In this manner, β , α and α'' are unambiguously discriminated via segmentation.

4.1 Data preparation

The phase segmentation method begins with the twice over reindexing of all EBSPs in the OI AZtec software suite. For the first map, both β and α are used to reindex the EBSPs (Figure 5, Map 1 in Step 1.b). The EBSD map data is exported from the *.oip and compressed data subfolder format of OI Aztec to the *.cpr and *.crc file format of OI Channel-5 (Figure 5, 1.c). The “TruMap” elemental maps are computed in OI Aztec and exported as comma separated value (csv) files (Figure 5, 1.c). “TruMaps” are elemental maps in the OI AZtec software suite that have been corrected for artefacts, elemental overlaps and X-ray background and therefore exhibit a clear and “true” contrast even for minor compositional variations. Since the segmentation method is not subject to the EDS-EBSD system of a

specific manufacturer, “TruMaps” are hereafter referred to as “processed EDS maps” in the following paragraphs.

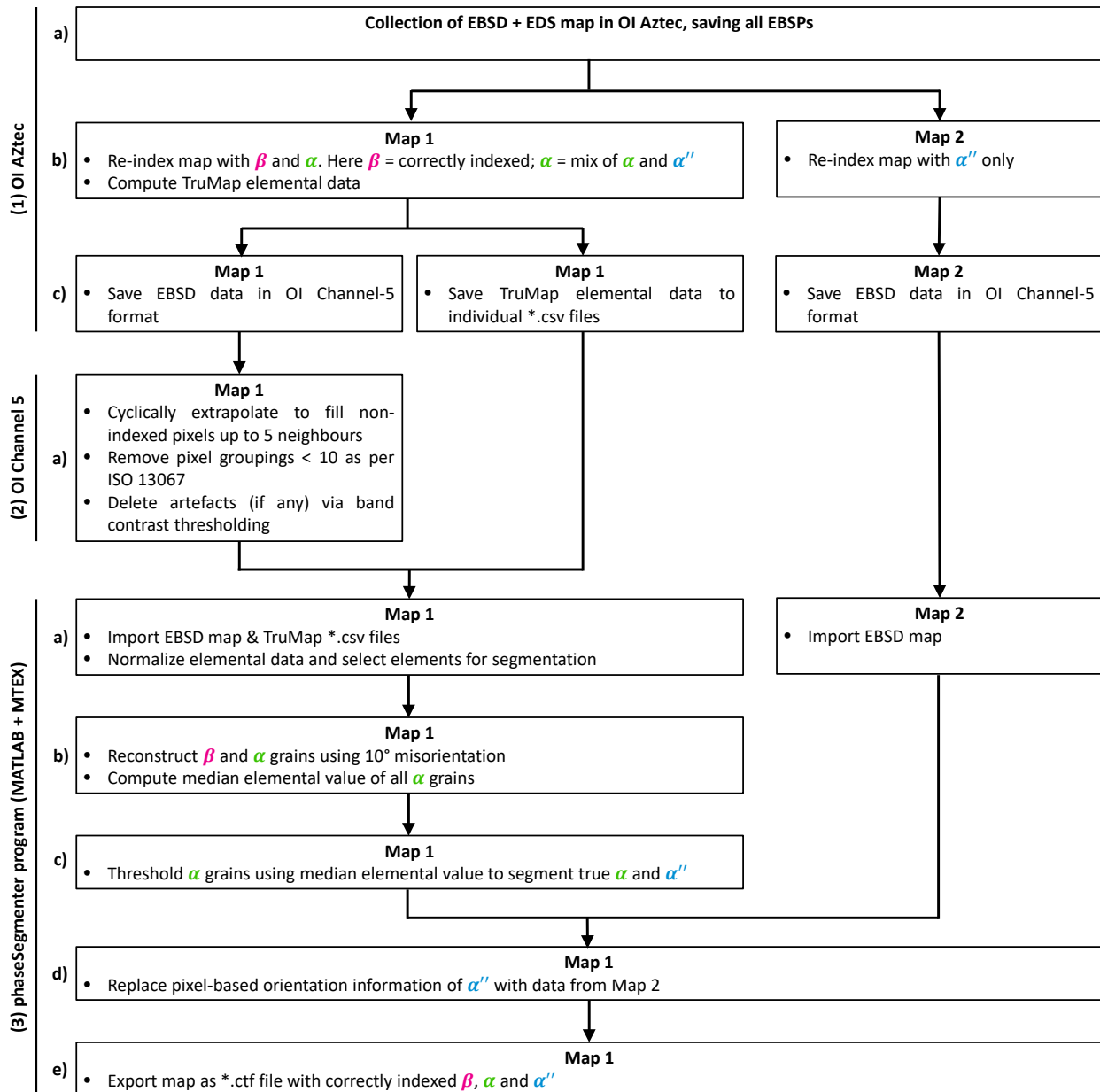


Figure 5: Detailed flowchart showing all the steps involved in this phase segmentation method. The process is subdivided into steps undertaken using: (1) OI AZtec (2) OI Channel-5, and (3) the MATLAB-based *phaseSegmenter* program.

Post-processing of the first EBSD map, containing α - and β -indexed orientation data, was undertaken in the OI Channel-5 software suite and comprised the iterative cyclic extrapolation to fill unindexed regions down to 5 neighbours, the removal of pixel groupings smaller than 10 as per the ISO 13067 recommendation and the removal of orientation data from regions with band contrast values < 35 (Figure 5, 2.a). For this map, the chosen band contrast threshold value excludes the data points that are obviously not indexable due to the localised contamination of the sample (see the black spot in Figure 1b). It follows that the threshold value is user-defined and is based on the band contrast of the artefacts (if any) contained within individual EBSD maps. Orientation extrapolation is justified in the present case, as analyses involving minor misorientations are not undertaken and downstream martensitic orientation variant analysis requires seamless boundary interfaces between adjacent, neighbouring grains. Following this, the first map is ready to be imported into the *phaseSegmenter* program (Figure 5, Map 1 in 3.a). The phase map of this processed first map is shown in Figure 6a.

For the second map, only α'' martensite is used to reindex the EBSPs (Figure 5, Map 2 in 1.b). This map is not post-processed before it is imported into the *phaseSegmenter* program (Figure 5, Map 2 in 3.a). The phase map of this second, unprocessed map is shown in Figure 6b.

4.1 Grain reconstruction

After the first map, containing both β and α indexed phases, is imported into the *phaseSegmenter* program (Figure 5, Map 1 in 3.a), the grains are reconstructed using the *calcGrains* command in MTEX. Here the processing options are the critical misorientation angle and the minimum grain area. A reasonable value for the critical misorientation angle is application dependent. In the present case, the β , α and α'' grains are well described using a 10° critical misorientation angle as all interfaces comprise high-angle boundaries. Since pixel groupings smaller than 10 were already removed beforehand in OI Channel-5, the minimum grain area criterion for the removal of small grains was not required (Figure 5, 3.b).

4.1 EDS channel selection and optimal threshold value determination

Upon importing the individual processed EDS maps into the *phaseSegmenter* program, the elemental data within 3 standard deviations from the mean (3σ limits) is mapped to a relative scale of 0 to 1; thereby cutting-off outlier pixels via saturation within each EDS elemental channel and normalising the intensity. The user is then prompted to select the elements (or channels) to be used for phase

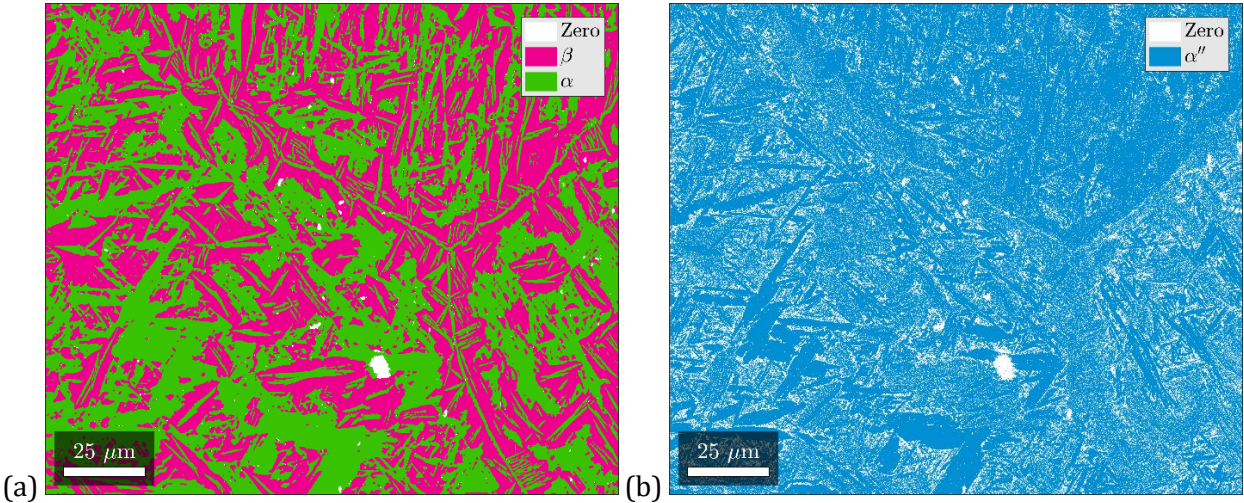


Figure 6: Phase maps of (a) Map 1 indexed using α and β after Step 2 in Figure 5 and (b) Map 2 indexed using α'' only after Step 1.c in Figure 5.

segmentation. As an alternative to the straight-forward selection of a single element, several EDS elemental channels can also be integrated into one processing channel. Moreover, the user has two further options that: (i) add inverted channels to make use of qualitatively inverse compositional profiles and/or, (ii) apply image filters that reduce noise and enhance contrast in the EDS elemental maps to further highlight the compositional differences between phases (Figure 5, 3.a).

Figure 7 shows the processed elemental maps of Ti, V, Fe and Al after importing as well as two processing channels P_1 and P_2 . P_1 comprises the normalised integrated intensities of Fe and V and the inverted Ti and Al processed elemental maps; P_2 is similar to P_1 but without the contribution of the inverted Ti signal. All elemental maps show a distinct contrast between α on the one hand and $\beta + \alpha''$ on the other. This is quantified by the approximate mean elemental difference between α and $\beta + \alpha''$ ($d\bar{x}$ in Figure 7). Between any of these elements, the difference is ≤ 3 at.%; which corresponds to an average difference of < 20 counts as discussed later in Section 4.6.

The Al and Fe signals yield reasonable phase contrast but appear noisier (*i.e.* with lower peak to background ratios) than the V and Ti elemental maps. The Ti elemental map appears to be sensitive to surface artefacts which are visible as dark features in the grayscale image. Consequently, the V elemental map is considered better suited for phase segmentation. Both processed channels, P_1 and

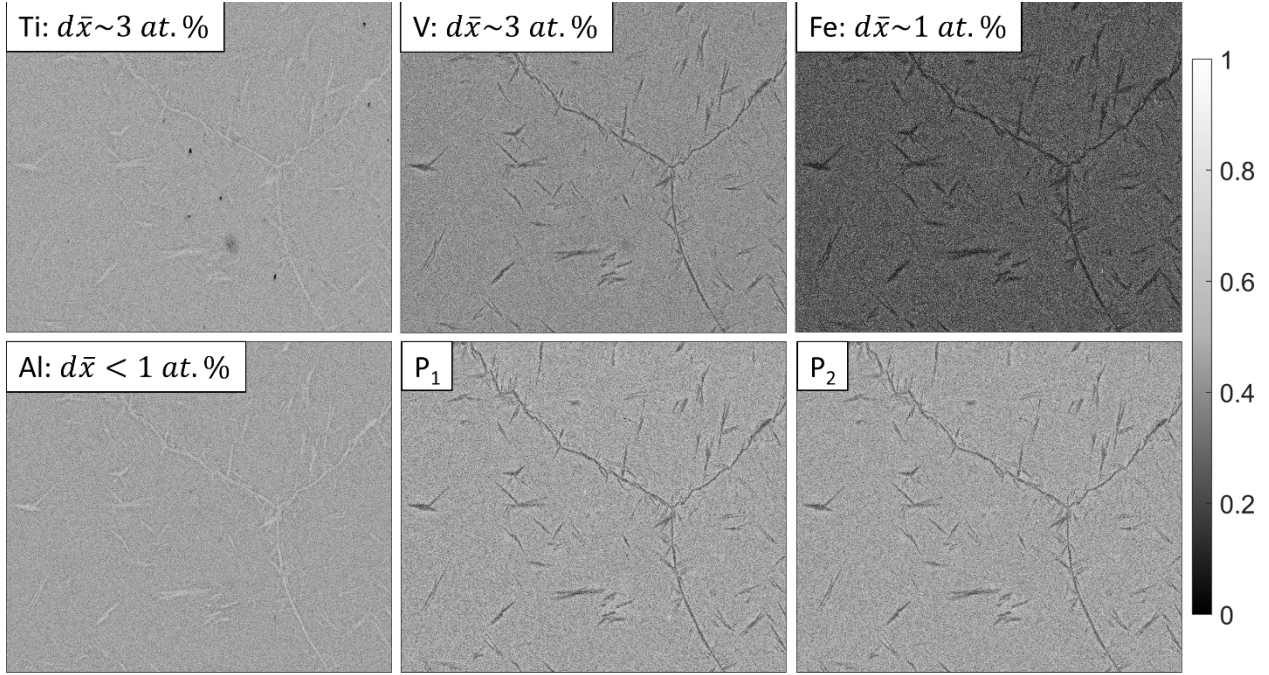


Figure 7: Normalised processed EDS maps showing the phase contrast between α and $\beta + \alpha''$ for different elemental channels and two processing channels P_1 and P_2 . The approximate average elemental differences between α and $\beta + \alpha''$ are indicated by $d\bar{x}$. Processing channel P_1 comprises the normalised integrated intensities of Fe and V and the inverted Ti and Al processed elemental maps. Processing channel P_2 comprises the normalised integrated intensities of Fe and V and the inverted Al processed elemental map.

P_2 lead to slight improvements in phase contrast over the V elemental map. Since the P_1 and P_2 maps reveal similar phase contrast and the artefacts in the Ti elemental map are inherited by the P_1 map, the P_2 map is also selected for phase segmentation. It follows that both, the P_2 and V maps are evaluated for their efficacy in enabling phase segmentation. In the present case, image filtering did not lead to improved phase segmentation. Denoising, smoothing and/or sharpening of the elemental maps might improve the visual contrast between phases but these filters manipulate the maps to an extent that the grain-median EDS contrast in the later part of phase segmentation is impeded.

The median values of the normalised V and P_2 counts were calculated for each of the α -indexed reconstructed grains (Figure 5, Step 3.b) of the first map in Figure 6a and are shown in Figure 8. The colour limits of these maps are defined by the standard deviation from the median value of the grain distribution (shown for the P_2 map in Figure 9). A standard deviation-based colour range was found

to consistently yield the ideal contrast between α and α'' martensite to enable manual threshold selection. The *phaseSegmenter* program allows for iterative refinement of the manually selected threshold value.

Automation of this step by curve fitting the frequency versus normalised elemental count distribution and finding the threshold value was attempted. However, this step was difficult to implement for all distribution types, as the ideal threshold value depends heavily on the selected channel and application in mind.

In the present case, segmentation with either the P_2 or the V elemental channel led to overall satisfactory phase segmentation. At first glance, the grain-median V signal in Figure 8b shows a stronger phase contrast, but this is solely on account of the varying colour scales. It was found that the grain-median P_2 signal in Figure 8a was less noisy and led to slight improvements in segmentation. Therefore, going forward, the P_2 map was selected for segmentation (Figure 5, 3.c).

In the present case, an optimal threshold value of 0.465 was found. The optimal threshold value is designated as τ and indicated by a dotted line in Figure 9. The plotted relative grain-median EDS count distribution shows a characteristic shoulder on the left side which is associated with the α phase. Figure 10a and b show the inverse pole figure maps with respect to the horizontal direction in the map of the α -indexed grains with relative grain-median counts of less than and greater than 0.465, respectively. Comparison with Figure 1a clearly shows that the grains in Figure 10a are α grains whereas the grains in Figure 10b belong to α'' martensite. The method does not segment all grains perfectly – some of the very small grains in Figure 10a may not belong to α and a few small α grains can also be found with the α'' grains in Figure 10b. However, for the majority of grains, the segmentation method is successful in discriminating α and α'' martensite. Depending on the alloy system and in order to more confidently discriminate between grain groups belonging to two phases, the optimal threshold value may be adjusted to shift the weight of the phase discrimination error towards one or the other of the grain groups.

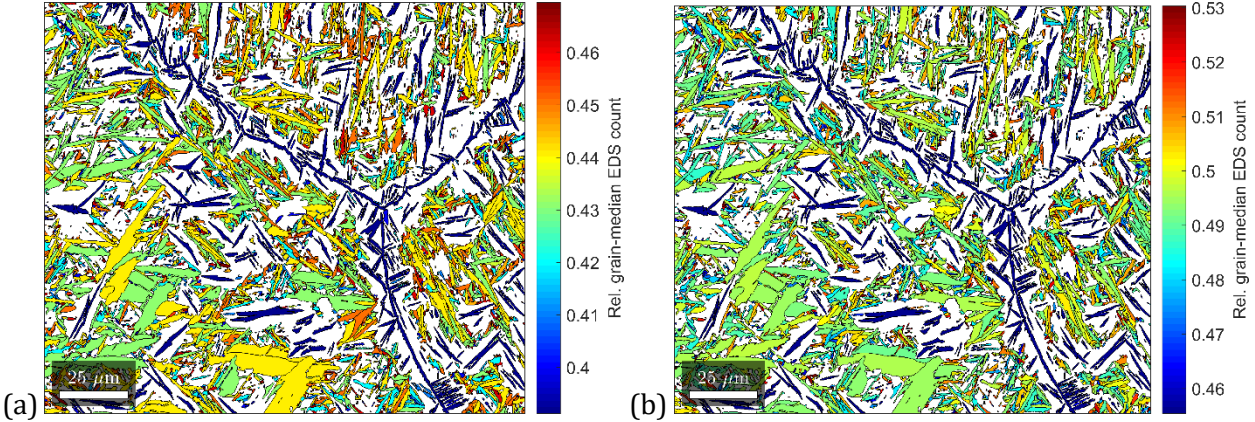


Figure 8: Relative grain-median EDS count of (a) V elemental channel and (b) processing channel P_2 (see Figure 7). The map in Figure 8b was used to segment α from α'' .

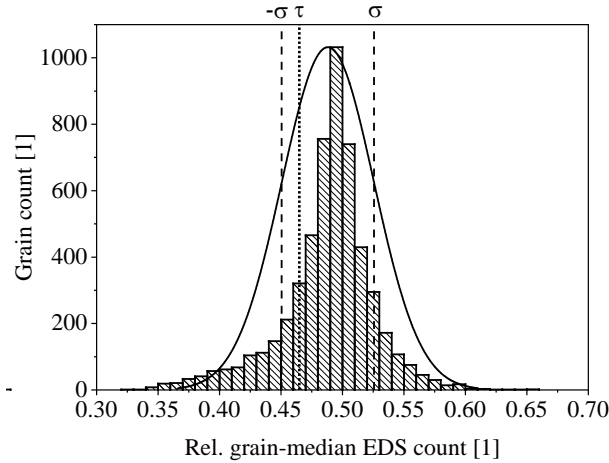


Figure 9: Histogram and normal distribution of the grain-median count of the P_2 processing channel. The standard deviation, σ , from the mean value defines the colour limits of the plot in Figure 8a (see interval formed by the dashed lines). The iteratively determined optimal threshold value, τ , of 0.465 is indicated by the dotted line.

4.1 Reindexing of α''

After segmenting the α -indexed pixels into groups associated with α and α'' martensite (Figure 10), the latter needs to be reassigned as α'' martensite (Figure 5, Step 2.c). Therefore the second map, reindexed using α'' martensite only (Figure 6b), is imported into the *phaseSegmenter* program (Figure 5, Map 2 in Step 3.a). The phase identification and orientation data of the pixels segmented as α'' martensite in the first map (EBSD data in Figure 10b) are now replaced with the data from the

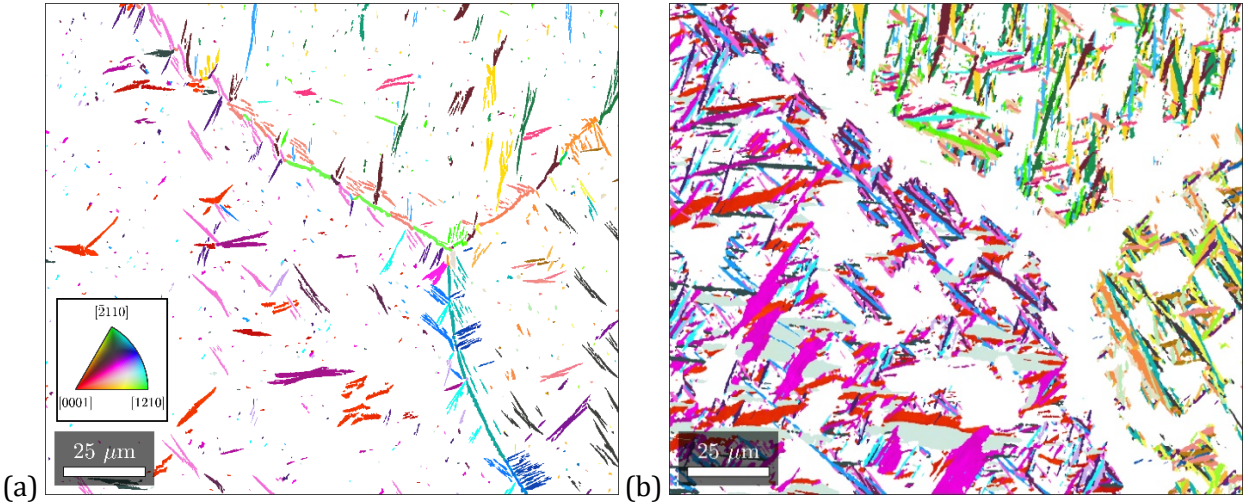


Figure 10: Inverse pole figure map of the α -indexed phase segmented at the optimal threshold of 0.465 of the relative grain-median EDS count (see map in Figure 8b and distribution in Figure 9) : (a) α grains belonging to α (b) α grains belonging to α'' . The grains in both maps are coloured according to the orientation colour key in Figure 10a.

second map (Figure 6b). Here the user can also choose whether or not unindexed points (or zero solutions) in the $\alpha + \beta$ map (Map 1) should be reassigned or not (Figure 5, 3.d). The final EBSD dataset consisting of correctly indexed β , α and α'' phases is then exported as a *.ctf file (Figure 5, 3.e). Following the procedure outlined in Section 4.2, the orientation data of α'' in the final EBSD dataset is processed as well.

4.2 Validation

The final β , α and α'' martensite phase map is shown in Figure 11a and the inverse pole-figure map of α'' martensite with respect to the horizontal direction in the map is given in Figure 11b. The phase fractions after phase segmentation are 48% β , 9% α and 42% α'' with $\sim 1\%$ unindexed points. Comparison of the maps in Figure 11 with the micrographs in Figure 1 confirms a satisfactory segmentation result.

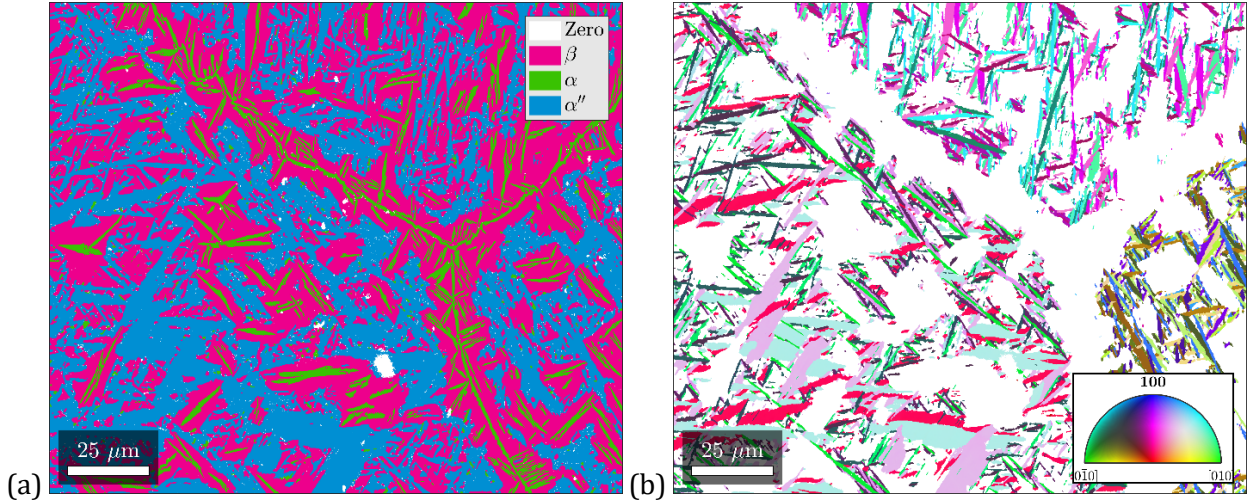


Figure 11: (a) Phase map after grain-median EDS-based phase segmentation with the *phaseSegmenter* program (b) Inverse pole figure map of α'' .

Figure 12 shows the relative frequency distributions of EDS counts in the discriminated β , α and α'' phases for elements Ti, V, Al and Fe. It is evident that the EDS count distributions of β and α'' are almost identical, whereas the EDS distribution of α is slightly shifted. The shift confirms that the phases were successfully segmented by their elemental distributions. The value for x_c in Figure 12 describes the refined peak centre position from a Gaussian fit. Between α and (β or α''), the absolute peak shift for all elements is between 5 and 20 counts. The relative peak shift, defined as the absolute peak shift divided by three standard deviations of the mean, amounts to 4.5 % for Ti, 13.8 % for V, 7.3 % for Al and 10.5 % for Fe. V reveals the largest relative peak shift, which is in line with this element being previously identified in Section 4.4 as the most suitable candidate for elemental thresholding. Between α'' and β , the relative peak shifts for all elements is ~ 1 %.

A pole figure of the α'' martensite orientation variants within the β grain located at the lower left of Figure 11 is shown in Figure 13 using the same IPF colour key as in Figure 11b. It is evident that the orientation data is neatly gathered around 6 clusters which are the α'' martensite orientation variants for this β grain with the average orientation $\phi_1 = 260^\circ$, $\Phi = 43^\circ$ and $\phi_2 = 28$. These respective validations confirm that segmentation was successful in unambiguously discriminating all three phases in the present metastable β -Ti alloy.

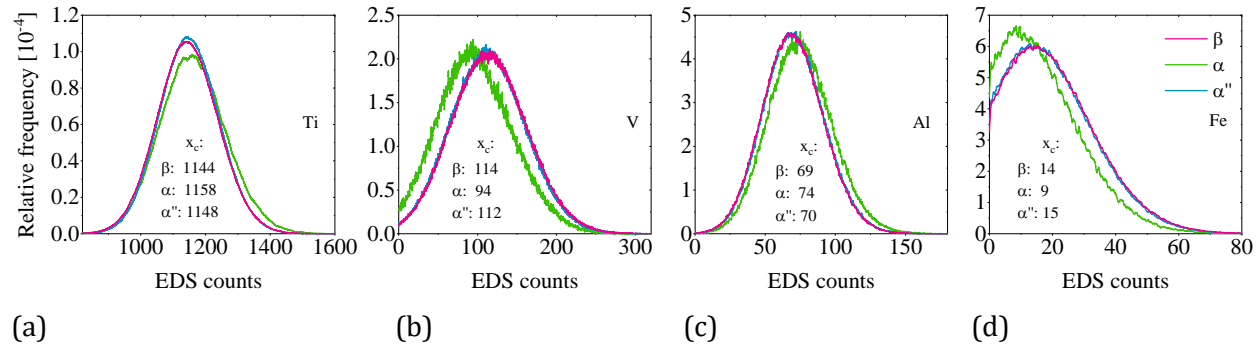


Figure 12: Relative frequency distributions of EDS counts in β , α and α'' for elements (a) Ti, (b) V, (c) Al and (d) Fe. x_c indicates the refined peak centre position from a Gaussian fit. It is evident that the centre positions for β and α'' are almost identical, whereas the centre position of α is slightly shifted.

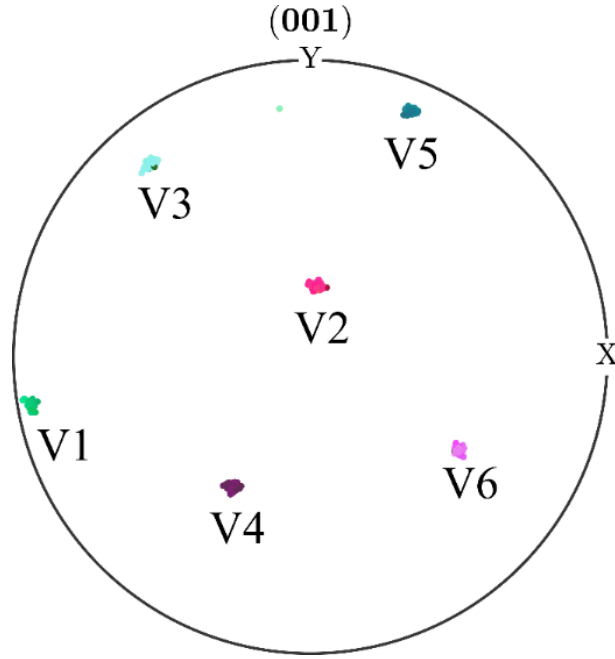


Figure 13: Pole-figure showing 1000 randomly chosen EBSD data points associated with the α'' orientation variants 1 to 6 from the lower left β grain in Figure 11 [$\phi_1 = 260^\circ$, $\Phi = 43^\circ$ and $\phi_2 = 28^\circ$]. The applied color key is identical to the one shown in Figure 11b.

5 Discussion

5.1 Advantages and limitations of the proposed segmentation method

Following image acquisition, EBSPs undergo 2D Hough transformation to identify and locate the Kikuchi bands based on their centres, edges or by applying more advanced, multi-step algorithms [42]. Thereafter, EBSPs are indexed by matching the interplanar Bragg angles of the experimental and theoretical Kikuchi bands. However, as described in Section 3.2.3, and regardless of the applied EBSP indexing algorithm, errors in phase discrimination occur when crystal structures are only distinguishable by marginal differences in unit cell volume rather than crystal symmetry and its associated interplanar angles. In such cases, the elemental differences between the phases can be exploited to discriminate them on-the-fly by undertaking simultaneous EDS-EBSD. Here reference spectra corresponding to the unique chemistries of each phase are pre-defined prior to mapping. The characteristic X-ray spectrum emitted at each dwell point during acquisition is then matched against the previously acquired reference spectra and the possible solutions ranked in order. Consequently, the ranking weighs the possible EBSD solutions which in turn, results in the accurate differentiation of crystallographically similar phases.

The above process of spectrum matching, which OI refers to as “TruPhase” [43,44], compares the full spectrum profile of an active point of interest with the pre-defined reference spectra even if both spectra contain noise and low counts; which is mostly the case during simultaneous EDS-EBSD mapping using the hardware configuration of this study. The method is nominally robust as it: (i) is insensitive to peak overlaps and changes in background intensity, (ii) is applied in real time during map acquisition and, (iii) can also be applied during post-processing by creating reference spectra and then reindexing stored EBSPs.

However, spectrum matching only works consistently when: (i) the reference spectra are distinct enough to effectively discriminate the two phases on-the-fly during map acquisition or, (ii) there are no elemental gradients[§] from grain boundaries to grain interiors in the two phases. In the present

[§] Elemental gradients could be associated with both actual diffusion gradients and/or signal gradients from the overlap of the electron interaction volume between adjacent grains.

case, the compositional differences between the α and $\beta + \alpha''$ phases for the four alloying elements are a few atomic percent (see Section 4.4) such that these marginal differences only become apparent upon generating quantitative elemental maps.

With respect to the last point, a quantitative elemental map (which OI refers to as “TruMap” [30]) can be generated either during live acquisition or when the pixel-based spectral data is post-processed using a technique OI refers to as “Tru-Q” [45] involving: (a) background suppression via the application of a top hat filter and, (b) peak deconvolution and separation via least-squares fitting, to construct quantitative elemental maps. However, the ability to use quantitative elemental maps for on-the-fly phase discrimination is not currently available. The only available option to discriminate phases during live EDS-EBSD map acquisition is the spectrum matching approach described above. It follows that the phase segmentation method detailed in Section 4 then becomes necessary.

Furthermore, since simultaneous EDS-EBSD mapping returns low elemental counts on account of the hardware used in this study, the post-processed elemental maps exhibit low peak to background ratios and are affected by signal gradients between grain boundaries and their interiors on account of sample tilt and/or thermo-mechanical processing history. In the former case, spatial resolution could pose a significant issue as X-ray data is generated from larger sample volumes and its point of origin is displaced slightly down the tilted plane of the sample relative to the point from where an EBSP is generated. In this scenario, individual point-by-point use of EDS data may suffer, especially when the microstructural features requiring discrimination are on the scale of $<5\text{ }\mu\text{m}$. While the above scenario is not observed in the present study, these real-world limitations could severely impede consistent, pixel-based phase discrimination. Consequently, the proposed phase segmentation method, with its primary feature being a median grain chemistry approach, is indispensable to successfully discriminate all phases.

While the segmentation method detailed in this paper is developed to consistently discriminate α , β and α'' in a metastable β Ti alloy, the method is equally applicable to any microstructure that exhibits n phases of undiscernible crystal structure (here α and α'') and $\geq n - 1$ of these phases exhibiting unique characteristics in their EDS signal (here α). As a grain-median method, a marginal difference in an alloying element is sufficient to segment and discriminate phases. Since this method relies on the computation of grains for segmentation, an important limitation is that the crystallographically undiscernible phases are required to form grains that are distinguishable by orientation only.

5.2 Alternative approaches to phase discrimination

The main disadvantage of the present methodology is that it is an involved approach that necessitates significant data storage, simultaneous acquisition of the EDS signal, the twice over offline reindexing of EBSPs and subsequent analysis using the MTEX toolbox using the functions developed in the work. While the suggested approach should be available to all researchers using relatively modern, commercial EBSD-EDS systems purchased in the last decade, researchers could consider other hardware and software approaches that offer different potential paths to effective phase discrimination.

The hardware approach involves using the latest generation EDS detectors that could enable the real-time discrimination between α and α'' for this class of Ti alloys. In this study, the 80 mm^2 X-Max EDS detector interfacing with the AZtec v4.1 acquisition software suite recorded an average spectrum count of 956. Alternatively, the latest generation, large area EDS systems are rated as processing upwards of 500,000 counts per second. It is surmised that at acquisition speeds of 40.5 Hz as used in this study, X-ray spectra containing $>10,000$ counts could be acquired at every analysis point. The sensitivity contained in the higher counts may then be enough to enable real-time discrimination between α and α'' .

Alternative software approaches include the use of the dictionary based EBSD indexing algorithm [46] or a modification of the projective Kikuchi pattern matching approach [47]. While the first software approach may provide equally effective phase discrimination without requiring the use of chemical information, the process suffers from a similarly intensive offline reindexing of EBSPs as this study. While the second software approach may be able to fit distorted EBSP simulations to experimentally acquired EBSPs and thereby provide the differences between α and α'' , higher quality experimental EBSPs are likely required for such analyses. In practical terms, this requirement necessitates either: (i) longer map acquisition times using the widely available, phosphor screen, CCD camera based EBSD detectors as used in this study or, (ii) the purchase of next generation, CMOS sensor based EBSD detectors with their significantly faster acquisition rates.

While newer software approaches provide alternatives, the authors emphasise a final point. As shown in Figure 3, conventional Hough transformation-based indexing of EBSPs returns both α and α'' as viable solutions because there is no discernible difference between these two phases along

their $[\bar{1}10]_{\alpha}$ and $[010]_{\alpha''}$ zone axes. In this peculiar circumstance, it may just be the case that regardless of the applied EBSP indexing technique, the use of EBSPs alone may be insufficient to distinguish α and α'' . It follows that the use of elemental information may prove indispensable when distinguishing these phases either during live acquisition or during downstream offline reprocessing via segmentation.

5.3 Applicability to Ti alloys

If the above conditions for the general applicability of the new phase segmentation method are met, it is capable of discriminating and segmenting the following phase combinations in Ti alloys : $\beta+\alpha+\alpha'$, $\beta+\alpha+\alpha''$ and $\beta+\alpha+\alpha_{massive}$. However, in microstructures that contain more than one of the phases α' , α'' and $\alpha_{massive}$ [24–26], phase discrimination using the present method reaches its limitation.

A suitable example where the new segmentation method can be readily applied is Ref. [48]. In that study, deformation-induced α' developed in an initially $\alpha+\beta$ microstructure. The authors indexed both α and α' as α and then manually discriminated α and α'' based on their morphologies. A second example where the new segmentation method can be applied is additively manufactured Ti microstructures. In this case, the high cooling rates commonly lead to the formation of α' which subsequently decomposes to α and β upon annealing with passive heat coming from the melting of adjacent regions. Similar to Ref. [48], the microstructure characterisation work in Refs. [49–51] also show both α and α' being indexed as α . The present method may aid the systematic analysis of such microstructures by reasonably accurate phase discrimination.

6 Conclusion

This study details that α'' martensite EBSPs are primarily misindexed as α because of an indiscernible difference between these phases along their $[\bar{1}10]_{\alpha}$ and $[010]_{\alpha''}$ zone axes. Since α and α'' show only slight compositional differences, on-the-fly phase discrimination using EDS spectrum matching is not feasible. Consequently, a segmentation method was developed that relies on a combination of reindexed EBSPs and grain-median EDS elemental data to unambiguously discriminate β , α and α'' martensite in metastable β -Ti alloys. The process of segmentation is explained in detail and is available as an open-source computer program called *phaseSegmenter* that makes use of the MTEX toolbox in MATLAB and is freely available via the link in Ref. [39]. The unambiguous discrimination

of α'' martensite enables its downstream orientation variant analysis which, in turn, will lead to improvements in the understanding of transformation-induced plasticity in metastable β -Ti alloys.

Acknowledgement

F. Niessen acknowledges the Danish Council for Independent Research grant DFF-8027-00009B for financial support. A. Gazder acknowledges the Australian Research Council - Discovery Project grant DP170100836 and the 2019 AIIM for Gold - Investigator grant. The JEOL JSM-7001F was funded by the Australian Research Council - Linkage, Infrastructure, Equipment and Facilities grant LE0882613. The Oxford Instruments 80 mm² X-Max EDS detector was funded via the 2012 UOW Major Equipment Grant scheme.

References

- [1] A. Savant, Titanium Metal Market Price Trend, Global Analysis, Size Estimation, Industry Share, Future Growth and Forecast 2019 to 2023, Reuters.Com. (2019). <https://www.marketresearchfuture.com/reports/titanium-metal-market-7482> (accessed July 16, 2019).
- [2] ScienceDirect, (2019). <https://www.sciencedirect.com/> (accessed July 16, 2019).
- [3] F.H. Froes, Powder metallurgy of titanium alloys, 2013. doi:10.1533/9780857098900.2.202.
- [4] B. Dutta, F.H. Froes, Additive manufacturing of titanium alloys, *Addit. Manuf. Handb. Prod. Dev. Def. Ind.* (2017) 263–274. doi:10.1201/9781315119106.
- [5] W. Greenwood, R.H. Johnson, The deformation of metals under small stresses during phase transformations, *Proc. R. Soc. A.* 283 (1965).
- [6] C.L. Magee, H.W. Paxton, Transformation kinetics, microplasticity and aging of martensite in Fe-31Ni, 1966.
- [7] J.B. Leblond, J. Devaux, J.C. Devaux, Mathematical modelling of transformation plasticity in steels 1: Case of ideal-plastic phases, *Int. J. Plast.* 5 (1989) 551–572.
- [8] S. Chatterjee, Transformations in TRIP-assisted Steels: Microstructure and Properties, 2006.
- [9] A. Kromm, S. Brauser, T. Kannengiesser, M. Rethmeier, High-energy synchrotron diffraction study of a transformation induced plasticity steel during tensile deformation, *J. Strain Anal. Eng. Des.* 46 (2011) 581–591. doi:10.1177/0309324711403969.
- [10] J. Yan, TRIP Titanium Alloy Design, Northwestern University, 2014.
- [11] F. Sun, J.Y. Zhang, M. Marteleur, T. Gloriant, P. Vermaut, D. Laillé, P. Castany, C. Curfs, P.J. Jacques, F. Prima, Investigation of early stage deformation mechanisms in a metastable β titanium alloy showing combined twinning-induced plasticity and transformation-induced plasticity effects, *Acta Mater.* 61 (2013) 6406–6417. doi:10.1016/j.actamat.2013.07.019.
- [12] C. Brozek, F. Sun, P. Vermaut, Y. Millet, A. Lenain, D. Embury, P.J. Jacques, F. Prima, A β -titanium alloy with extra high strain-hardening rate: Design and mechanical properties, *Scr. Mater.* 114 (2016) 60–64. doi:10.1016/j.scriptamat.2015.11.020.

- [13] S. Sadeghpour, S.M. Abbasi, M. Morakabati, A. Kisko, L.P. Karjalainen, D.A. Porter, A new multi-element beta titanium alloy with a high yield strength exhibiting transformation and twinning induced plasticity effects, *Scr. Mater.* 145 (2018) 104–108. doi:10.1016/j.scriptamat.2017.10.017.
- [14] M.I. Latypov, S. Shin, B.C. De Cooman, H. Seop, Micromechanical finite element analysis of strain partitioning in multiphase medium manganese TWIP + TRIP steel, *Acta Mater.* 108 (2016) 219–228. doi:10.1016/j.actamat.2016.02.001.
- [15] J. Mola, B.C. De Cooman, Quenching and partitioning processing of transformable ferritic stainless steels, *Scr. Mater.* 65 (2011) 834–837. doi:10.1016/j.scriptamat.2011.07.041.
- [16] L. Yuan, D. Ponge, J. Wittig, P. Choi, J.A. Jiménez, D. Raabe, Nanoscale austenite reversion through partitioning, segregation and kinetic freezing: Example of a ductile 2 GPa Fe-Cr-C steel, *Acta Mater.* 60 (2012) 2790–2804. doi:10.1016/j.actamat.2012.01.045.
- [17] M. Karlsen, J. Hjelen, Ø. Grong, G. Rørvik, R. Chiron, U. Schubert, E. Nilsen, SEM/EBSD based in situ studies of deformation induced phase transformations in supermartensitic stainless steels, *Mater. Sci. Technol.* 24 (2008) 64–72. doi:10.1179/174328407X245797.
- [18] B. Verlinden, P. Bocher, E. Girault, E. Aernoudt, Austenite texture and bainite/austenite orientation relationships in TRIP steel, *Scr. Mater.* 45 (2001) 909–916. doi:10.1016/S1359-6462(01)01110-1.
- [19] H. Wang, Y. Jeong, B. Clausen, Y. Liu, R.J. McCabe, F. Barlat, C.N. Tomé, Effect of martensitic phase transformation on the behavior of 304 austenitic stainless steel under tension, *Mater. Sci. Eng. A*. 649 (2016) 174–183. doi:10.1016/j.msea.2015.09.108.
- [20] L. Ryde, Application of EBSD to analysis of microstructures in commercial steels, *Mater. Sci. Technol.* 22 (2006) 1297–1306. doi:10.1179/174328406x130948.
- [21] K. Zhu, D. Barbier, T. Iung, Characterization and quantification methods of complex BCC matrix microstructures in advanced high strength steels, *J. Mater. Sci.* 48 (2013) 413–423. doi:10.1007/s10853-012-6756-9.
- [22] T. Waterschoot, L. Kestens, B.C. De Cooman, Hot rolling texture development in CMnCrSi dual-phase steels, *Metall. Mater. Trans. A Phys. Metall. Mater. Sci.* 33 (2002) 1091–1102.

doi:10.1007/s11661-002-0211-5.

- [23] A.A. Gazder, F. Al-Harbi, H.T. Spanke, D.R.G. Mitchell, E. V. Pereloma, A correlative approach to segmenting phases and ferrite morphologies in transformation-induced plasticity steel using electron back-scattering diffraction and energy dispersive X-ray spectroscopy, *Ultramicroscopy*. 147 (2014) 114–132. doi:10.1016/j.ultramic.2014.07.005.
- [24] M. Marteleur, F. Sun, T. Gloriant, P. Vermaut, P.J. Jacques, F. Prima, On the design of new β -metastable titanium alloys with improved work hardening rate thanks to simultaneous TRIP and TWIP effects, *Scr. Mater.* 66 (2012) 749–752. doi:10.1016/j.scriptamat.2012.01.049.
- [25] K. Wei, Z. Wang, F. Li, H. Zhang, X. Zeng, Densification behavior, microstructure evolution, and mechanical performances of selective laser melted Ti-5Al-2.5Sn α titanium alloy: Effect of laser energy input, *J. Alloys Compd.* 774 (2019) 1024–1035. doi:10.1016/j.jallcom.2018.09.153.
- [26] Z. Liu, S.L. Lu, H.P. Tang, M. Qian, L. Zhan, Characterization and decompositional crystallography of the massive phase grains in an additively-manufactured Ti-6Al-4V alloy, *Mater. Charact.* 127 (2017) 146–152. doi:10.1016/j.matchar.2017.01.012.
- [27] S.L. Lu, M. Qian, H.P. Tang, M. Yan, J. Wang, D.H. StJohn, Massive transformation in Ti-6Al-4V additively manufactured by selective electron beam melting, *Acta Mater.* 104 (2016) 303–311. doi:10.1016/j.actamat.2015.11.011.
- [28] Y.W. Chai, H.Y. Kim, H. Hosoda, S. Miyazaki, Self-accommodation in Ti-Nb shape memory alloys, *Acta Mater.* 57 (2009) 4054–4064. doi:10.1016/j.actamat.2009.04.051.
- [29] B. Sundman, U.R. Kattner, M. Palumbo, S.G. Fries, OpenCalphad - a free thermodynamic software, *Integr. Mater. Manuf. Innov.* 4 (2015) 1. doi:10.1186/s40192-014-0029-1.
- [30] Oxford Instruments, Application note “TruMap: Real time - real results,” 2011.
- [31] H.-J. Bunge, *Texture Analysis in Materials Science: Mathematical Methods*, Butterworths, 1982.
- [32] K. Mukherjee, M. Kato, Lattice Correspondance and Crystallography of Martensites in Titanium Alloys, *Le J. Phys. Colloq.* 43 (1982) C4-297-C4-302. doi:10.1051/jphyscol:1982441.

- [33] G. Lütjering, J. C. Williams, Titanium, (2007). doi:10.1007/978-3-540-73036-1.
- [34] T. Inamura, J.I. Kim, H.Y. Kim, H. Hosoda, K. Wakashima, S. Miyazaki, Composition dependent crystallography of α'' -martensite in Ti-Nb-based β -titanium alloy, Philos. Mag. 87 (2007) 3325–3350. doi:10.1080/14786430601003874.
- [35] R. Davis, H.M. Flower, D.R.F. West, Martensitic transformations in Ti-Mo alloys, J. Mater. Sci. 14 (1979) 712–722. doi:10.1007/BF00772735.
- [36] H.Y. Kim, L. Wei, S. Kobayashi, M. Tahara, S. Miyazaki, Nanodomain structure and its effect on abnormal thermal expansion behavior of a Ti-23Nb-2Zr-0.7Ta-1.2O alloy, Acta Mater. 61 (2013) 4874–4886. doi:10.1016/j.actamat.2013.04.060.
- [37] M. Klinger, A. Jäger, Crystallographic Tool Box (CrysTBox): Automated tools for transmission electron microscopists and crystallographers, J. Appl. Crystallogr. 48 (2015) 2012–2018. doi:10.1107/S1600576715017252.
- [38] T. Maitland, S. Sitzman, Electron Backscatter Diffraction (EBSD) Technique and Materials Characterization Examples, in: W. Zhou, Z.L. Wang (Eds.), Scanning Microsc. Nanotechnology. Tech. Appl., Springer Verlag, New York, 2007: pp. 41–75.
- [39] F. Niessen, phaseSegmenter [Software] Freely available from <https://github.com/frankNiessen/phaseSegmenter>, (2019).
- [40] MathWorks, MATLAB 2016b (9.1.0.441655), (2016).
- [41] F. Bachmann, R. Hielscher, H. Schaeben, Texture Analysis with MTEX – Free and Open Source Software Toolbox, Solid State Phenom. 160 (2010) 63–68. doi:10.4028/www.scientific.net/SSP.160.63.
- [42] K. Thomsen, N.H. Schmidt, A. Bewick, K. Larsen, J. Goulden, Improving the Accuracy of Orientation Measurements using EBSD, Microsc. Microanal. 19 (2013) 724–725. doi:10.1017/s1431927613005618.
- [43] J. Goulden, S. Sitzman, K. Larsen, R. Jones, Real-Time Discrimination of Phases with Similar Kikuchi patterns but Different Chemistry through Simultaneous EBSD and EDS, Microsc. Microanal. 21 (2015) 2033–2034. doi:10.1017/s1431927615010946.

- [44] J. Goulden, K. Larsen, R. Jones, S. Sitzman, Real-time discrimination of phases with similar Kikuchi patterns but different chemistries through simultaneous EBSD and EDS, 2015.
- [45] Oxford Instruments, Application note “Tru-Q™ – Making Accurate Analysis a Reality for All Introduction,” 2011.
- [46] Y.H. Chen, S.U. Park, D. Wei, G. Newstadt, M.A. Jackson, J.P. Simmons, M. De Graef, A.O. Hero, A Dictionary Approach to Electron Backscatter Diffraction Indexing, *Microsc. Microanal.* 21 (2015) 739–752. doi:10.1017/S1431927615000756.
- [47] A. Winkelmann, G. Nolze, G. Cios, T. Tokarski, Mapping of local lattice parameter ratios by projective Kikuchi pattern matching, *Phys. Rev. Mater.* 2 (2018) 1–7. doi:10.1103/PhysRevMaterials.2.123803.
- [48] S.W. Lee, J.M. Oh, C.H. Park, J.K. Hong, J.T. Yeom, Deformation mechanism of metastable titanium alloy showing stress-induced α' -Martensitic transformation, *J. Alloys Compd.* 782 (2019) 427–432. doi:10.1016/j.jallcom.2018.12.160.
- [49] M. Wang, H.Q. Li, D.J. Lou, C.X. Qin, J. Jiang, X.Y. Fang, Y.B. Guo, Microstructure anisotropy and its implication in mechanical properties of biomedical titanium alloy processed by electron beam melting, *Mater. Sci. Eng. A.* 743 (2019) 123–137. doi:10.1016/j.msea.2018.11.038.
- [50] D.W. Wang, Y.H. Zhou, J. Shen, Y. Liu, D.F. Li, Q. Zhou, G. Sha, P. Xu, T. Ebel, M. Yan, Selective laser melting under the reactive atmosphere: A convenient and efficient approach to fabricate ultrahigh strength commercially pure titanium without sacrificing ductility, *Mater. Sci. Eng. A.* 762 (2019) 138078. doi:10.1016/j.msea.2019.138078.
- [51] X. Wang, K. Chou, EBSD study of beam speed effects on Ti-6Al-4V alloy by powder bed electron beam additive manufacturing, *J. Alloys Compd.* 748 (2018) 236–244. doi:10.1016/j.jallcom.2018.03.173.